LLNL-JRNL-832838

LAWRENCE LIVERMORE NATIONAL LABORATORY

Chemical Modifications of Ag Catalyst Surfaces with Imidazolium Ionomers Modulate H2 Evolution Rates during Electrochemical CO2 Reduction

D. M. Koshy, S. A. Akhade, A. Shugar, K. Abiose, J. Shi, S. Liang, J. S. Oakdale, S. E. Weitzner, J. B. Varley, E. B. Duoss, S. E. Baker, C. Hahn, Z. Bao, T. F. Jaramillo

March 16, 2022

Chemical Modifications of Ag Catalyst Surfaces with Imidazolium Ionomers Modulate H2 Evolution Rates during Electrochemical CO2 Reduction

Disclaimer

Chemical modifications of Ag catalyst surfaces with imidazolium-ionomers modulate H_2 evolution rates during electrochemical CO_2 reduction

David M. Koshy[1,2], Sneha A. Akhade[3], Adam Shugar[1], Kabir Abiose[2,4], Jingwei Shi[1], Siwei Liang[3], James S. Oakdale[3], Stephen E. Weitzner[3], Joel B. Varley[3], Eric B. Duoss[3], Sarah E. Baker[3], Christopher Hahn[2,3,*], Zhenan Bao[1,2,*], Thomas F. Jaramillo[1,2,*]

* Denotes corresponding authors

1. Department of Chemical Engineering, Stanford University, Stanford, CA 94305 USA

2. SUNCAT Center for Interface Science and Catalysis, SLAC National Accelerator Laboratory, Menlo Park, CA 94025 USA

3. Materials Sciences Division, Lawrence Livermore National Laboratory, Livermore, CA 94550 USA

4. Department of Mechanical Engineering, Stanford University, Stanford, CA 94305 USA

Abstract

Bridging polymer design with catalyst surface science is a promising direction for tuning and optimizing electrochemical reactors that could impact long-term goals in energy and sustainability. Particularly, the interaction between inorganic catalyst surfaces and organic-based ionomers provides an avenue to both steer reaction selectivity and promote activity. Here, we studied the role of imidazolium-based ionomers for electrocatalytic CO_2 reduction to CO (CO_2R) on Ag surfaces and found that they produce no effect on CO_2R activity yet strongly promote the competing hydrogen evolution reaction (HER). By examining the dependence of HER and CO_2R rates on concentrations of CO_2 and HCO_3^-, we developed a kinetic model that attributes HER promotion to intrinsic promotion of HCO_3^- reduction by imidazolium-ionomers. We also show that varying the ionomer structure by changing substituents on the imidazolium ring modulates the HER promotion. This ionomer-structure dependence was analyzed via Taft steric parameters and density functional theory calculations which suggest that steric bulk from functionalities on the imidazolium ring reduces access of the ionomer to both HCO_3^- and the Ag surface thus limiting the promotional effect. Our results help develop design rules for ionomer-catalyst interactions in CO_2R and motivate further work into precisely uncovering the interplay between primary and secondary coordination in determining electrocatalytic behavior.

Introduction

Polymer science is motivated by the highly tunable properties that macromolecules exhibit based on subtle changes to chemical structure, conformation, and chain length.[1] By leveraging precise synthetic chemistry, polymers can be designed with specific functionalities in mind and can then be rationally optimized for diverse applications including structural components, electronic materials, and medicine.[2–4] In the field of heterogeneous catalysis, polymers are most commonly implemented as ionomers, ion-containing polymers, that bind electrocatalyst layers and facilitate ion transport.[5] Most synthetic polymer design for electrocatalysis has focused on optimizing either cationic or anionic conductivity for a desired application.[6,7]

We propose that designing ionomer structures for electrochemical applications can be expanded to also include direct promotion of the intrinsic kinetics of an electrocatalytic surface. Because ionomers necessarily form an interface with catalyst surfaces, they are present directly in the reaction layer and could tune kinetics via non-covalent interactions with reactants, adsorbates, or products. Precedent for this hypothesis is seen in the fields of enzymatic catalysis and homogeneous catalysis where, in addition to the primary coordination to the catalytic active site, the secondary coordination sphere can also strongly impact catalyst performance.[8,9] This secondary sphere is comprised of the environment around the catalytic site that does not directly participate in covalent bonding, can also strongly impact catalyst performance.[8,9] These non-covalent, secondary sphere interactions, often referred to as the catalytic microenvironment[10,11], have been shown to help stabilize intermediates and improve catalytic activity but are difficult to study in heterogeneous catalysis due to the lack of catalytic sites that are well-defined on the atomic scale.

As a case study, we selected electrochemical reduction of CO_2 (CO_2R) as a reaction of interest where the ability for ionomer layers to steer activity and selectivity could greatly impact future industrial applications. CO_2R is motivated by the urgent need for renewable and sustainable energy technologies because it converts CO_2 to value-added products such as CO, ethanol, or ethylene at ambient conditions by applying an electric potential driving force.[12] To this point, controlling reaction selectivity within the distribution of CO_2R products as well as selectivity versus the competing hydrogen evolution reaction (HER) has been a major challenge. Thus, there is a significant opportunity to modulate reaction selectivity through careful design of the reaction microenvironment, directly at the catalyst-electrolyte interface. We propose that the combination of polymer design and synthesis and electrocatalytic testing can result in a tuned, hybrid interface that improves catalytic performance.

The direct influence of ionomers on catalytic activity has been most well-studied for the oxygen reduction reaction (ORR) where perfluorosulfonic acid polymers (e.g. Nafion) electrostatically adsorb to Pt surfaces and reduce available surface area for catalysis.[13] However, recent results show that many organic-based additives can influence the activity of CO_2R electrocatalysts suggesting that tuned, non-covalent interactions could be used to engineer improved catalytic performance and thus, more efficient CO_2R systems.[14] In CO_2R, various polymer systems have been shown to influence activity including polyethyleneimine acting as a co-catalyst for formate production[15], electropolymerized pyridinium films on Ag for HER suppression[16], promotion of CO production on Co Pc sites by pyridine-containing polymers[17], and, notably, imidazolium-containing polymers developed by Dioxide Materials under the brand name Sustainion.[18,19]

These commercialized imidazolium-ionomers are attached to a polystyrene backbone and have been shown to yield high selectivity for CO_2R to CO on Ag surfaces when used as a membrane in membrane electrode assembly (MEA) tests.[19] These results, as well as kinetic and spectroscopic investigations of imidazolium ionic liquid additives in CO_2R in acetonitrile, have suggested that imidazolium-ionomers promote CO_2R through specific non-covalent interactions with CO_2 or CO_2R intermediates.[20–22] However, despite the interesting catalytic results reported in this system, there is a lack of studies that systematically vary the chemical structure of an ionomer and report resulting aqueous CO_2R activity which has prevented the elucidation of design rules that govern the influence of ionomers on the intrinsic kinetics of heterogeneous catalysts.

Efforts to form these relationships include recent work on pyridinium-based films which suggested that functionalized pyridiniums lead to tunable stabilization of adsorbed CO* and thus improved ethylene selectivity on Cu.[23,24] In addition, a tri-component ionomer containing imidazolium, pyridinium, and fluoromethyl-phenyl groups was reported to synergistically suppress HER and promote ethylene selectivity on Cu through a variety of effects including hydrophobicity, transport improvements, and electric field effects.[25] Conversely, another report maximized the activity of Cu for ethylene through solely transport improvements achieved by interfacing the catalyst layer with thin perfluorosulfonic-acid polymer layers.[26] These studies represent advances in our understanding of structure-property relationships in ionomer design for Cu-catalyzed CO_2R; however, the complexity of CO_2R kinetics on Cu make it challenging to make concrete conclusions about the effect of ionomers on specific steps in the CO_2R mechanism. Thus, a well-defined, model system is necessary to study ionomer-catalyst interactions in CO_2R and make mechanistic claims about the role of ionomers in directing intrinsic CO_2R activity.

In this study, we investigated the effect of thin films of imidazolium-ionomers on the intrinsic kinetics of Ag for CO_2R and HER. By focusing on Ag, a catalyst surface known to predominantly produce CO and H_2 under CO_2R conditions, and using a benchmarked, two-compartment electrochemical cell we could more easily deconvolute transport and activation control for both HER and CO_2R.[27,28] We employed ultrathin films, ~3 nm, of ionomer to ensure contact and interaction between the Ag catalyst and the ionomer but minimize ohmic or transport losses which would otherwise convolute kinetic measurements. In addition, our ionomer synthesis strategy keeps the ionic content and chain length of the polymer constant while varying the structure of the imidazolium ionic group, thus allowing us to isolate the effect of ionomer chemical structure on CO_2R kinetics.

Methods

Ionomer Synthesis: Ionomers were synthesized in two-steps according to literature procedures: first involving the polymerization of styrene and chloromethylstyrene to form the intermediate copolymer and second exchanging the chloride group with a desired imidazole to form the imidazolium-containing ionomers.[19]

Styrene-chloromethylstyrene copolymer synthesis: Styrene (≥99%, Sigma-Aldrich) and 4-(chloromethyl)styrene (90%, Sigma-Aldrich) were first purified in a basic Al_2O_3 column to remove the radical inhibitor. Then, styrene (10.06 g, 96 mmol) and 4-(chloromethyl)styrene (6.23 g, 41 mmol) were mixed in chlorobenzene (15 mL) with azoisobutyronitrile (0.161 g, 1 mmol) and stirred at 70^{o}C for 12 hrs. The resulting solution was precipitated in stirred methanol (100 ml) to yield a white, powdered solid that was collected through filtration and redissolved in dimethylformamide (DMF) before being re-precipitated two more times into excess of methanol for purification. Finally, the collected white solid was dried in an oven at 100^{o}C. The final product had a number average molecular weight of 32 kDa by GPC, NMR integration confirming 30% incorporation of chloromethylstyrene monomer is available in Supporting Information.

Imidazole exchange: The intermediate copolymer (1 g) was dissolved in DMF (6 mL) along with a 1-substituted imidazole (7 mmol, 2.75 eq to (chloromethyl)styrene groups). Imidazoles tested here were: 1-methylimidazole (99%, Sigma-Aldrich), 1,2-dimethylimidazole (97%, Sigma-Aldrich), 1-butylimidazole (98%, Sigma-Aldrich), 1-tertbutylimidazole (98%, TCI America, Fisher Scientific), and 1-benzylimidazole (99%, Sigma-Aldrich). The solution was stirred at

110°C for 46 hrs before precipitating in ethyl ether with centrifugation at 10,000 rpm to precipitate the polymer. After another redissolution in DMF and precipitation + centrifugation in ethyl ether, the final orange-brown polymer was dried overnight at 100°C in an oven. NMR showed negligible peak intensity at ~4.6 ppm corresponding to Ar-CH_2-Cl from the styrene-chloromethylstyrene copolymer confirming the exchange reaction effectively to completion for all imidazoles (NMR peak assignment available in **SI-Figure 2-6**).

Electrode Preparation: Ag foil (1 mm, 99.9985%, Alfa Aesar), was polished with 5 μM, 1 μM, and 0.05 μM alumina polishing slurries (Ted Pella, Inc.) and sonicated in DI water for 30 minutes before each experiment. In a typical experiment, an ionomer solution consisting of 1 mL ethanol and 6.25 μL of 0.5 mg/mL ionomer stock solution (synthesized using dry polymer dissolved in ethanol) was manually spray coated (Speedaire 4RR09J, 30 psi, N_2) onto the Ag foil to synthesize an ionomer film. We note that residual DMF from the ionomers on the electrode was minimized by the diluted ionomer solution (3.125 μg/mL) and evaporation induced by spray coating.

Electrochemical CO_2R Testing: CO_2R testing was performed in a 2-compartment, PEEK, electrochemical cell reported previously.[27] Briefly, two electrolyte chambers (1.8 mL each, 0.1 $KHCO_3$) are separated by an anion exchange membrane (Selemion AMV; AGC) with a glassy carbon (2 mm, Alfa Aesar) counter electrode on the anolyte side and working Ag foil on catholyte side with potential control using a Ag/AgCl reference electrode (ET072-1, eDAQ). Both chambers were bubbled with CO_2 through a glass fritted inlet (10 sccm) and the catholyte gas outlet was routed to an in-line gas chromatograph (SRI Instruments; 8610C) for quantification of CO with the FID detector and H_2 with the TCD detector. In a typical experiment, chronoamperometry scans were run for 30 minutes per potential with two GC injections per potential. The electrochemical CO_2R results reported here are averages of two separate experiments, each containing ~12 chronoamperometric measurements with the averaged results interpolated to yield smooth current-voltage profiles. Potentials reported were corrected manually for solution resistance (~50 Ω) measured by electrochemical impedance spectroscopy.

For the CO_2 rate order experiments, the total inlet flowrate was maintained at 20 sccm with a CO_2/N_2 mixture where the ratios were adjusted to achieve a series of CO_2 partial pressures between 0 and 1 bar. For the $KHCO_3$ rate order experiments, the total ionic concentration was maintained at 1M with a $KHCO_3$/KCl mixture where the molar ratios were adjusted to achieve a series of $KHCO_3$ concentrations between 0.25 and 1 M. In both rate order experiments, a single injection from a 7.5 minute chronoamperometry scan was used to quantify product formation rates at each electrode potential.

Rotating disk electrode (RDE) testing was performed in 0.1 M $KHCO_3$ with a graphite rod anode, Ag/AgCl reference electrode (Accumet), and an Ag disk insert working electrode. Prior to testing, the Ag disk was polished with the same series of alumina polishing steps as for Ag foil and sonicated for 30 minutes in DI H_2O. Ag disk was spray coated to achieve identical ionomer loading of 0.5 μg/cm^2.

Characterization: Ellipsometry was performed on 1MPS (1-methylimidazolium on polystyrene) coated on a Si wafer at 0.5 μg/cm^2 (same loading as used in the Ag CO_2R experiments), and the film thickness was quantified using a Si + Cauchy model layer for the polymer film (J. A. Woollam Co. α-SE spectroscopic ellipsometer). X-ray photoelectron spectroscopy (XPS, PHI Versaprobe 3, 1486.6 eV) was performed to measure N 1s and Cl 2p signal from thin ionomer films. Gel-permeation chromatography (GPC) analysis was performed using a Tosoh EcoSEC Ambient (Room Temp)-GPC equipped with two TSK gel GPC columns (G3000Hhr and G4000Hhr; 7.8 mm I.D. × 30 cm, 5 μm). The GPC was calibrated with a conventional calibration curve using monodisperse polystyrene standards with THF as a carrier solvent and a polymer solution at 1.5 mg/mL in THF.

Kinetic Model: The steady-state matrix as described in the manuscript and supporting information was used as the input fit function to fit the CO_2R data of bare Ag and Ag-1MPS using the *lsqcurvefit* function implemented in MATLAB R2016B. This procedure yielded relatively low variation from the inputted initial guess parameters so significant manual optimization was performed to reach reasonable values for the adjustable parameters before fitting yielded the reported curves.

Simulation Methods: Electronic structure calculations were performed using a plane-wave pseudopotential code using the Vienna *ab initio* simulation package (VASP v. 5.4.4)[29,30] with the Projector Augmented Wave method[31] for core valence treatment. The Kohn-Sham equations were solved self-consistently employing the revised Perdew-Burke-Ernzerhof (RPBE)[32] exchange-correlation functional described within the generalized gradient approximation (GGA).[33] The plane-wave basis set cutoff energy of 400 eV was adopted. The Methfessel-Paxton scheme was used for Fermi level smearing using a Gaussian width (σ) of 0.1 eV for the electrode surface.[34] The self-consistent electronic convergence limit was set to 1×10^{-5} eV while the ionic convergence limit for unconstrained atoms was set to 0.02 eV Å^{-1}. A periodic 8x8 asymmetric surface slab consisting of 4 layers with 15 Å vacuum region was constructed to model the Ag (100) surface. The Brillouin zone was sampled using only the Γ-point, which was sufficiently accurate for unit cells of over 250 atoms. Grimme's DFT-D3 approach[35] was employed to account for long-range dispersion (van der Waals) interactions using $s_8 = 0.51$ and $s_{R,6} = 0.87$ values for the RPBE-based damping function parameters. The VASPsol package was used to describe the solvent electrolyte with the dielectric constant for water set to a relative permittivity value of 80. A Debye length of 9.7 Å was used, corresponding to an electrolyte concentration of 0.1 M solution.[36,37] To simulate electrochemical conditions, the calculations adopted a full-Hessian correction method within the VASPsol calculator that allowed calculations to be performed within the framework of a grand canonical ensemble with a reservoir of electrons.[38] The number of electrons were treated as an additional degree of freedom as part of structural optimization thereby enabling evaluation of potential-controlled DFT enthalpies. Thus, the resulting reaction enthalpy (H) was evaluated simultaneously as a function of the atomic positions in Cartesian coordinates (r) and the number of electrons (n) using the **Eq. 1** using the total internal energy (E), the total number of nuclear charges in the system (n_0) and an effective energy level for the reference electrode (φ).[38] The effective energy level for the reference electrode (φ) is converted to an applied voltage (U) on the standard hydrogen electrode (SHE) scale as shown in **Eq. 2**, using a reference potential value of $\varphi_0 = -4.6$ eV for the SHE. The chemical potential of the electron (μ_e) can be thus derived as a function of the effective energy level of the reference electrode (φ) and the Fermi level of the working electrode (E_F) using **Eq. 3**. We refer the reader to reference 38 for comprehensive details of the methodology.

$$H(r,n) = E(r,n) - (n - n_0)\varphi \qquad \textbf{Eq. 1}$$

$$\varphi = -U + \varphi_0/e \qquad \textbf{Eq. 2}$$

$$\mu_e = (E_F - \varphi_0)/e + U \qquad \textbf{Eq. 3}$$

Structural optimization of the surface bound adsorbate species (HCO_3, CO_3 and H) was performed on the Ag (100) surface in the low coverage limit and the lowest energy stable configuration was selected for computing reaction energies. Based on the site favorability analyses, hydrogen was observed to adsorb most favorably in a hollow configuration while bicarbonate and carbonate species preferred to bind in a bidentate mode via Ag-O bonds. To estimate the effect of the ionomer additives, structural optimizations of the adsorbates were performed in conjunction using a charged styrene-imidazolium model of the ionomer near the Ag (100) electrode surface that was initially pre-optimized (**SI-Figure 13**). The styrene-imidazolium molecule containing either 1-methylimidazole or 1-tertbutylimidazole was considered in this study. The model was truncated beyond one styrene monomer unit and excluded the full backbone or multiple monomers of the ionomer chain for the sake of maintaining computational tractability. The effect of conformational variation on reaction energetics associated with multiple styrene monomer units or the polymer backbone is not considered in this study. Molecular dynamics-based evaluation should likely be considered in future assessments for deeper consideration of the complex interplay between the structural topography of the polymer and the ionomer functionalities that may influence the reaction energetics of HER.

The free energies of the adsorbates were computed by including zero-point energy (ZPE) based entropy and heat capacity corrections to the 0 K DFT electronic energies. The vibrational frequencies were calculated by including all degrees of freedom for the adsorbate and assumed no significant changes in the vibrational states of the Ag surface. The harmonic oscillator approximation at standard conditions of temperature and pressure was applied to treat the computed vibrations. To computationally assess the viability of HCO_3 as a proton donor, the Ag (100) mediated deprotonation of bicarbonate (**Eq. 4**) was considered and its corresponding reaction free energy (ΔG_{RXN}) (**Eq. 5**) was computed. The reaction free energies were calculated both in the absence and presence of the imidazolium monomer additive to investigate the influence of the additive in promoting bicarbonate deprotonation. The relative order-of-magnitude variation in reaction rates towards bicarbonate protonation due to the presence of the ionomer additive was quantified as a relative ratio of the Boltzmann factors as shown in **Eq. 6.**

$$HCO_3^* \rightarrow H^* + CO_3^* \qquad \textbf{Eq. 4}$$

$$\Delta G_{RXN}(U) = G_{CO3*\,+H*}(U) - G_{HCO3*}\,(U) \qquad \textbf{Eq. 5}$$

$$RE(U) = \frac{\exp\left(\frac{-\Delta G_{ionomer}(U)}{k_B T}\right)}{\exp\left(\frac{-\Delta G_{no\ ionomer}(U)}{k_B T}\right)} \quad \textbf{Eq. 6}$$

Here, $\Delta G(U)$ denotes the reaction free energy change as a function of applied electrode potential (U), k_B is the Boltzmann constant and T is the absolute temperature. We assume that the prefactors for bicarbonate deprotonation in **Eq. 6** are similar in magnitude in the presence and absence of the ionomer additive following which **Eq. 6** can reasonably provide qualitative trends in selectivity towards bicarbonate deprotonation across different ionomer additives considered in this study.

Results and Discussion

Ionomer Synthesis and Characterization

The ionomer synthesis used in this work directly followed the literature for Sustainion which employed a two-step process (**Fig 1A**).[19] First, styrene and 4-(chloromethyl)styrene were polymerized to form an intermediate polystyrene-based polymer with a certain fraction of the styrene monomers containing chloride groups. Next, substituted imidazoles were exchanged onto the intermediate polymer to produce heterogenized, cationic imidazolium groups on the polystyrene backbone. A single batch of the intermediate polymer was synthesized, containing 30 mol% of the chloromethylstyrene monomer by ^{1}H NMR and with a number-averaged molecular weight of 32 kDa and a polydispersity index of 1.6 by gel permeation chromatography corresponding to an average length of ~270 monomers. Then, all imidazolium-ionomers were grafted onto subsets of this same batch of intermediate polymer which ensured that the ionic content and chain length were identical which eliminates these factors when comparing their effect on CO_2R activity. In this study, 1-methylimidazole, 1,2-dimethylimidazole, 1-tertbutylimidazole, 1-butylimidazole, and 1-benzylimidazole were grafted and designated 1MPS, 12DMPS, 1tBPS, 1BPS, and 1BzPS respectively (**Fig 1B**). All imidazole exchanges went to completion based on the removal of the -CH_2-Cl NMR peaks and resulted in the expected chemical structure as confirmed by ^{1}H NMR and comparison to prior literature (**SI-Figure 1-7**).[39] All ionomers were soluble in ethanol and stock ionomer solutions were prepared for further use on CO_2R electrodes.

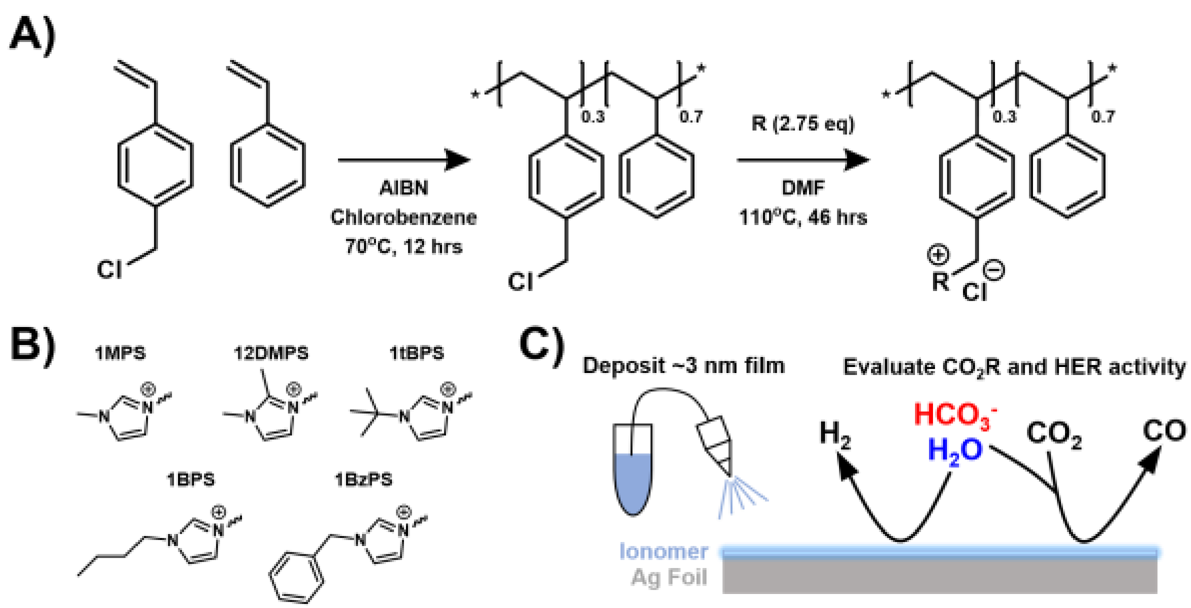

Figure 1. (A) Synthetic scheme for imidazolium-ionomers (B) Structures for the five imidazolium groups tested, connected to the polystyrene backbone at the wavy bond and with abbreviations denoted above corresponding structure and (C) Schematic of experimental approach showing deposition of thin ionomer film on Ag foil by spray coating and subsequent CO_2R testing.

Effect of imidazolium-ionomers on CO_2R and HER over Ag foil

Next, we tested the effects of these imidazolium-ionomers on CO_2R activity. These experiments were designed to ensure that a reproducible and uniform ionomer-catalyst interface was created while avoiding thick polymer layers that would hinder reactant or ionic transport to the catalyst surface.[40] In addition, we aimed to be able to make concrete statements about intrinsic activity in the presence of ionomers which necessitated a well-defined catalyst surface and simplified reaction pathways. To achieve these goals, we employed ultrathin layers of ionomer on Ag foil to ensure the interaction of imidazolium-groups with the catalyst surface and to work with a CO_2R system that predominantly makes CO via CO_2R and H_2 via HER and thus does not need liquid product analysis, significantly speeding up the experimental process (**Fig 1C**). These ionomer layers were spray coated from dilute (~3 μg/mL) ionomer solutions onto Ag foil at loadings of 0.5 $\mu g/cm^2$. Based on the bulk density of polystyrene, this would correspond to film thicknesses of ~3-4 nm which agrees with ellipsometry experiments that showed thicknesses of 3 ± 0.5 nm. X-ray photoelectron spectroscopy revealed subtle features at the N1s and Cl 2p regions both before and after electrochemical CO_2R testing that do not conclusively demonstrate the stability of the ionomer but show that either the ionomer or its decomposition products remain at the Ag surface throughout testing (**SI-Figure 7**). The decomposition of imidazolium moieties is known under alkaline conditions[41] and future work is necessary to ascertain the rate of degradation of these ionomers under the near-neutral pH electrochemical conditions employed here.

The initial CO_2R testing of 1-methylimidazolium on polystyrene (Ag-1MPS) immediately revealed that the imidazolium moiety did not promote the intrinsic reaction kinetics of CO_2R on Ag. The addition of 1MPS effectively left j_{CO} unchanged throughout the low overpotential, activation-controlled region through to the mass-transport limited current densities at high overpotential (**Fig 2A**). This result is in stark contrast to prior reports suggesting that imidazolium could intrinsically promote CO_2R on Ag surfaces.[20–22] This lack of agreement could stem from the fact that the previous studies that revealed promotion of CO_2R by imidazolium moieties were performed in non-aqueous environments. Thus, the existence of the polar, aqueous solvent environment might result in significantly different kinetic behavior on Ag that is unaffected by the presence of imidazolium. In addition, promotion of CO_2R was observed on Ag in mixed imidazolium ionic liquid-water electrolytes[42] suggesting that the polymeric nature of these ionomers could also play a role in promoting HER instead of CO_2R.

Despite the lack of observable effect to CO_2R to CO kinetics, the 1MPS layer did significantly promote the competing hydrogen evolution reaction relative to bare Ag (**Fig 2B**). In the low overpotential region, between -0.7 V and -1 V vs RHE, Ag-1MPS showed a significant increase in j_{H2} by ~4x relative to bare Ag at -0.9 V vs RHE. Increasing the 1MPS loading from 0.5 μg/cm^2 (**Fig 2A, 2B**) to 5 μg/cm^2 and 50 μg/cm^2 increased the HER promotion effect (**SI-Figure 8A**). However, at these higher loadings the j_{CO} curve is affected likely due to transport limitations induced by thicker polymer layers (**SI-Figure 8B**) so the lowest 0.5 μg/cm^2 loading was focused on for the remainder of the study.

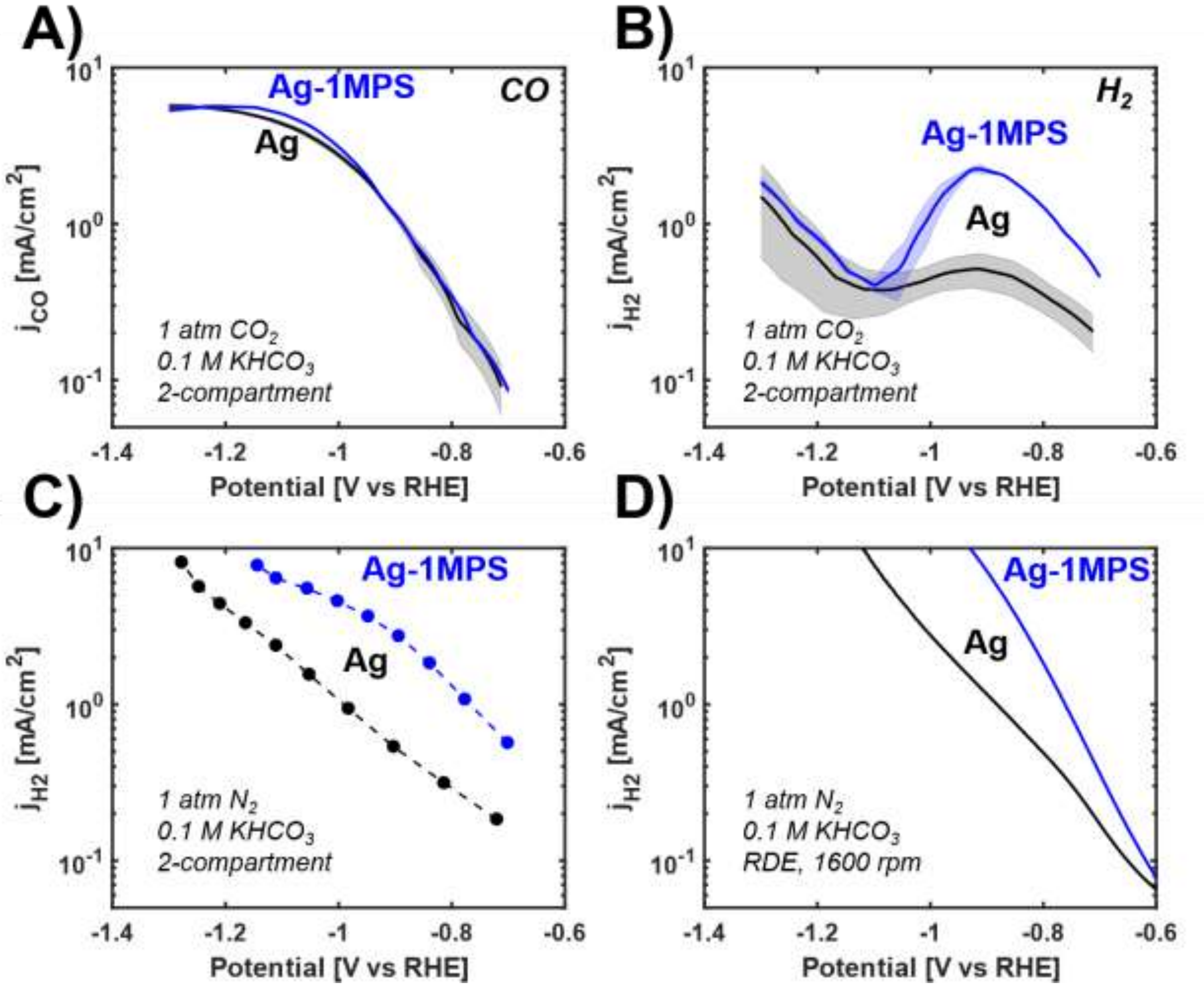

Figure 2. (A) Partial current density to CO (j_{CO}, logscale) versus electrode potential for bare Ag surface (Ag, black) and 0.5 μg/cm^2 of 1MPS on Ag (Ag-1MPS, blue) with shaded minimum/maximum error bars with corresponding partial current density to H_2 (j_{H2}, logscale) in (B). CO_2R experiments performed in 0.1M $KHCO_3$ with 10 sccm CO_2 inlet flowrate. Continuous curves in (A) and (B) were generated by interpolation of discrete chronoamperometric scans from two independent experiments (see Methods) (C) Comparison of j_{H2} for bare Ag (black) and Ag-1MPS (blue) in 2-compartment testing with N_2 flow with circles representing data from chronoamperometric scans and interpolated dash line to guide the eye and (D) Comparison of j_{H2} for bare Ag (black) and Ag-1MPS (blue) in rotating disk electrode testing with N_2 flow.

This striking promotion of HER on Ag manifests in a non-monotonic j_{H2}-voltage profile. First, j_{H2} rose to a maximum at -0.9 V vs RHE, then declined until -1.1 V vs RHE where it increased again and regains exponential, Tafel-like behavior and coincides again with the bare Ag j_{H2} curve (**Fig 2B**). To determine whether this HER promotion was an intrinsic effect, two control experiments were conducted. First, the same experiment was performed in the 2-compartment electrochemical cell with N_2 atmosphere instead of CO_2 to mitigate concurrent CO_2R turnover on Ag (**Fig 2C**). In this case, the Ag-1MPS electrode still showed significantly higher HER current than the bare Ag electrode. We note that no CO was detected by gas chromatography during this experiment, therefore all current from N_2 atmosphere experiments is attributed to the HER, within detection limits. To rule out a transport effect where the 1MPS layer facilitates faster proton donor transport, these N_2 atmosphere experiments were repeated in a rotating-disk electrode (RDE) rotating at 1600 rpm (**Fig 2D**). Again, the Ag-1MPS electrode showed higher current density demonstrating that the promotion of HER in the presence of 1MPS was present in both stagnant (2-compartment) and RDE configurations. This suggests that higher transport rates of possible proton donors (e.g. bicarbonate) through the thin polymer layer relative to the bare interface were unlikely to account for the observed differences in j_{H2}.

Origin of non-monotonic HER j-V profile

Though Ag-1MPS showed higher HER current than bare Ag under both CO_2 and N_2 atmospheres, a clear non-monotonic "bump" in j_{H2} present in the CO_2R experiments was no longer observed in the N_2 atmosphere experiments (**Fig 2B, 2C**). These different characteristics prompted us to elucidate the origin of the non-monotonic HER current observed under CO_2R conditions.

First, we observed that though the presence of the non-monotonic feature was more obvious in the Ag-1MPS j_{H2} curve that it was still present, though smaller, on bare Ag (**Fig 2B**). This demonstrates that the chemical mechanism for the non-monotonic HER feature is independent of the presence of an ionomer layer and is instead a fundamental characteristic of CO_2R on Ag and is exacerbated by the presence of the ionomer. Prior studies have reported this feature as well as its disappearance in the absence of CO_2 (in agreement with the results described above) and attributed the feature to the formation of adsorbed CO on Ag that inhibited HER.[43,44] This mechanism could decrease HER current if, for example, CO* desorption and H* adsorption were rate limiting for CO_2R and HER respectively, then adsorbed CO would rapidly fill most available active sites which would reduce HER current due to lack of available sites. However, this mechanism is unlikely because neither CO_2 adsorption or surface CO_2* hydrogenations are expected to be rate-limiting on relatively weak-binding surfaces like Ag[44] suggesting that an alternate explanation exists to explain the non-monotonic HER profile.

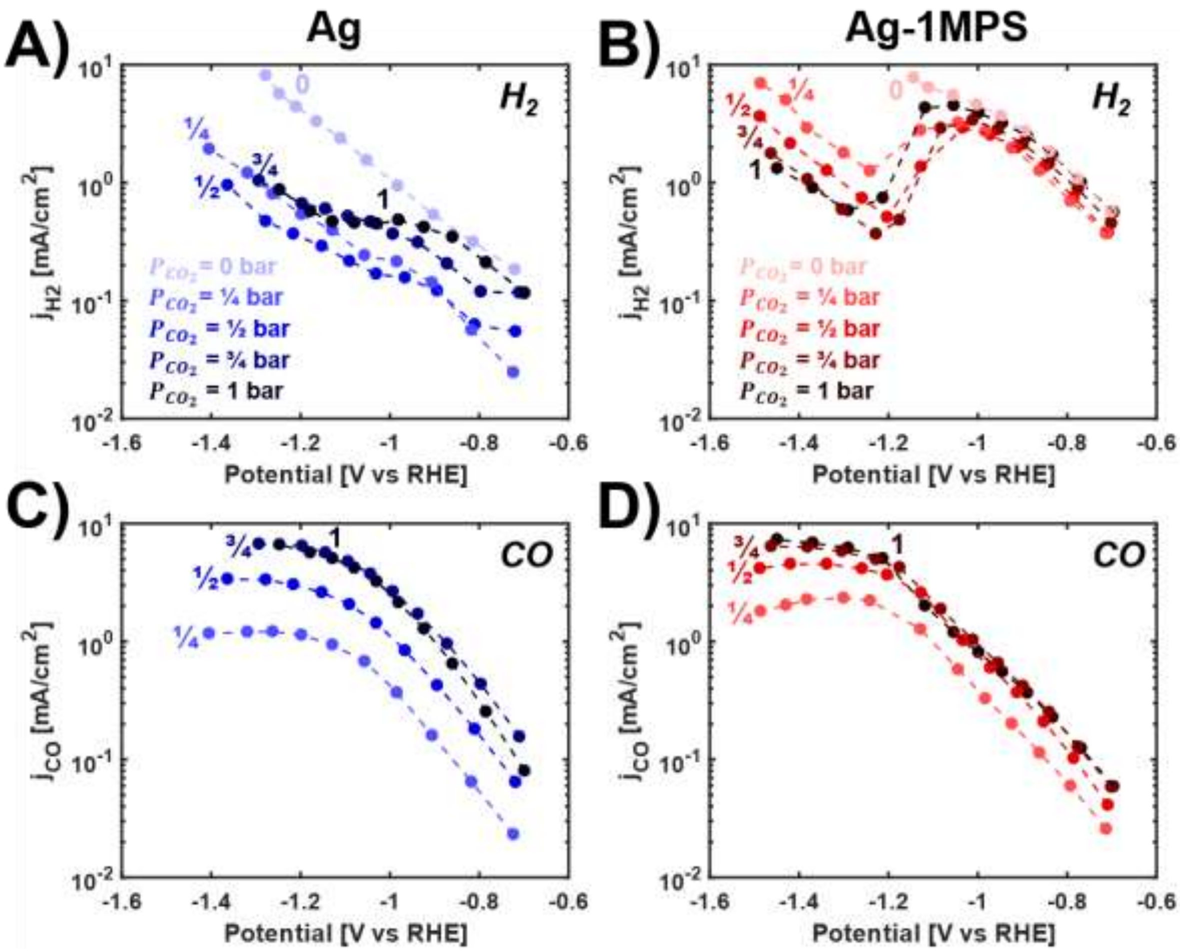

Figure 3. Partial current densities to H_2 (j_{H2}, logscale) vs electrode potential for a series of partial pressure of CO_2 between 0 and 1 bar (denoted by shading) for bare Ag (A) and Ag-1MPS (B) with corresponding CO partial current densities for bare Ag (C) and Ag-1MPS (D). All experiments in 2-compartment cell in 0.1M $KHCO_3$ with total flowrate set at 20 sccm.

To mechanistically probe this phenomenon, we performed concentration-dependent measurements to find the dependence of CO_2R and HER rates as a function of both partial pressure of CO_2 and concentration of the bicarbonate anion (HCO_3^-) on both bare Ag and Ag-1MPS electrodes. The P_{CO2} dependence experiments demonstrate that the concurrent evolution of CO on Ag directly affects the shape of the HER curves on both bare Ag and Ag-1MPS electrodes (**Fig 3A, 3B**). We note that the effect of changing partial pressure of CO_2 resulted in expected changes to the j_{CO} profiles on both electrodes with a reduction in both the transport-limited current density and reduced current at lower overpotential further suggesting that CO_2 adsorption is kinetically relevant (**Fig 3C, 3D**). The HER curves on bare Ag reveal that the small “bump” in HER present at P_{CO2} = 1 bar gradually smooths out as P_{CO2} is reduced until at P_{CO2} = 0 bar where a linear, Tafel-like HER curve is measured (**Fig 3A**). This trend is more apparent on the Ag-1MPS electrode where the ionomer-induced promotion of HER makes the “bump” very prominent and its disappearance can be observed as P_{CO2} is reduced from 1 bar to 0 bar (**Fig 3B**).

These results confirm that the non-monotonic HER profile on Ag is directly tied to concurrent turnover of CO_2R but does not explicitly point to which steps in the two reaction pathways are interconnected. Bicarbonate rate order experiments were conducted to assess how the concentration of a viable proton donor, HCO_3^-, affects the rates of HER and CO_2R on the Ag and Ag-1MPS electrodes (**Fig 4A-D**). Interestingly, we found that varying [HCO_3^-] between 0.25 M and 1 M (using KCl as a supporting electrolyte to maintain total ionic concentration at 1 M) produced no measurable effect to CO production rates for either electrode (**Fig 4C, 4D**). However, HER rates increased monotonically with increasing HCO_3^- concentration on both bare Ag and Ag-1MPS, particularly at lower overpotentials near the non-monotonic “bump”/plateau regime before largely converging at higher overpotentials (**Fig 4A, 4B**). This shows that HCO_3^- is a viable proton donor during CO_2R, in agreement with prior studies, and provides two conclusions about CO_2R kinetics on Ag. First, CO_2R to CO on Ag does not have a kinetically relevant proton transfer step, leading to no dependence on HCO_3^- concentration. Second, HCO_3^- is more energetically favorable to use as a proton donor than H_2O and thus is predominant at low overpotentials.[45,46]

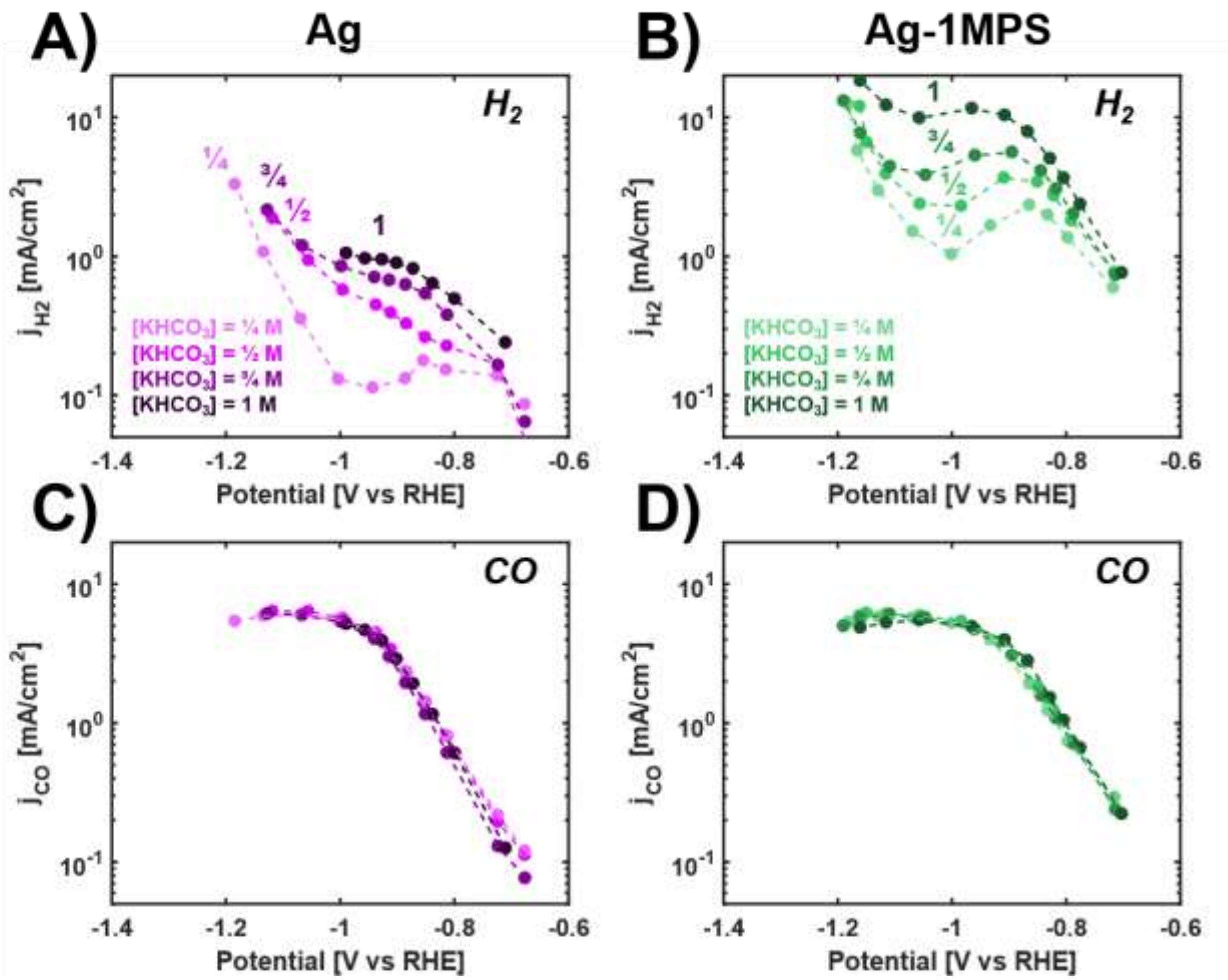

Figure 4. Partial current densities to H_2 (j_{H2}, logscale) vs electrode potential for a series of $KHCO_3$ concentrations between 0.25 M and 1 M (denoted by shading) for bare Ag (A) and Ag-1MPS (B) with corresponding CO partial current densities for bare Ag (C) and Ag-1MPS (D). All experiments in 2-compartment cell with 1 bar CO_2 and total ionic concentration set at 1M.

With the mechanistic insight from the P_{CO2} and HCO_3^- concentration dependence experiments, we can formulate a revised hypothesis on the kinetic regimes for HER during CO_2R on Ag. First, at low overpotentials near -0.7 V to -0.9 V vs RHE, both CO_2R and HER use HCO_3^- as a proton donor leading to linear, Tafel HER curves and dependence of HER on $[HCO_3^-]$ and no dependence of CO_2R on $[HCO_3^-]$ due to rate-limiting CO_2 adsorption. Next, at intermediate overpotentials near -0.9 V to -1.1 V vs RHE, increased CO_2R and HER current consumes HCO_3^- leading to a depletion of $[HCO_3^-]$ near the surface that becomes kinetically distinguishable for HER and manifests as a decrease in current due to lack of available proton donors. This does not result in noticeable changes to the j_{CO} curve because of the hypothesized CO_2 adsorption rate-limiting step that does not involve proton transfer.[44] Finally, at higher overpotentials near -1.3 V vs RHE, both H_2O and HCO_3^- are available as proton donors and the proton donor transport limitation is relieved which allows the reappearance of Tafel HER behavior. This explanation also predicts the absence of the non-monotonic HER feature in the absence of concurrent CO_2R because the consumption of HCO_3^- by the CO_2R pathway induces the critical transport limitation. In addition, this proposed mechanism would suggest that the primary effect of adding the 1MPS imidazolium-ionomer layer is to increase HER rates at low overpotential by increasing the rate constant of proton transfer from HCO_3^- which would yield a larger “bump” than bare Ag but still converge to Tafel HER behavior at high overpotentials where H_2O becomes a dominant proton donor.

To assess the validity of this hypothesized mechanism, we built a simple kinetic model for CO_2R and HER that incorporated transport terms for HCO_3^- and CO_2 (T_{CO2}, T_{HCO3}) and kinetic terms for CO_2R and HER that use either HCO_3^- (r_1, r_3) or H_2O (r_2, r_4) as the proton donor.

T_{CO2}	$CO_2^o \rightarrow CO_2$	$\frac{D_{CO_2}}{\delta}([CO_2^o] - [CO_2])$
T_{HCO3}	$HCO_3^{-o} \rightarrow HCO_3^-$	$\frac{D_{HCO_3^-}}{\delta}([HCO_3^{-o}] - [HCO_3^-])$
r_1	$HCO_3^- + e^- \rightarrow \frac{1}{2}H_2$	$k_1 e^{\eta\alpha_1 F/RT}[HCO_3^-]$
r_2	$H_2O + e^- \rightarrow \frac{1}{2}H_2$	$k_2 e^{\eta\alpha_2 F/RT}$
r_3	$2HCO_3^- + \mathrm{e}^- + CO_2 \rightarrow CO$	$k_3 e^{\eta\alpha_3 F/RT}[CO_2]$
r_4	$2H_2O + \mathrm{e}^- + CO_2 \rightarrow CO$	$k_4 e^{\eta\alpha_4 F/RT}[CO_2]$
r_5	$CO_2 + OH^- \rightarrow HCO_3^-$	$k_5[CO_2][OH^-] - k_{n5}[HCO_3^-]$

Here, D_x, [X], and [X^o] refer to the diffusion coefficient, surface concentration, and bulk concentration of a species X, δ was set at 202 μm for the boundary layer thickness (value chosen to achieve the correct limiting j_{CO} of 5.6 mA/cm^2 based on equation for T_{CO2}) that determines diffusive transport flux of both reactants (T_{CO2}, T_{HCO3}) , and Butler-Volmer expressions were used to simulate the effect of electrode potential on rate constants for electron transfer steps (r_1-r_4). This model does not explicitly calculate surface coverages of relevant intermediates and is instead intended to capture the interdependence of CO_2R and HER rates by using an assumption of the rate-determining step (RDS) for each reaction. Thus, we chose the initial proton transfer from HCO_3^-/H_2O as the RDS for HER (r_1, r_2) and the adsorption of CO_2 as the RDS for CO_2R (r_3, r_4) which is supported by our previous P_{CO2}/[HCO_3^-] dependence experiments. These reaction equations (r_1-r_4) are not explicitly stoichiometrically balanced and are intended to indicate the relevant species that are in the rate-determining steps and species being consumed in the CO_2R and HER pathways. After incorporating the homogeneous reaction between CO_2 and OH^- to produce HCO_3^- (r_5), we could solve for steady state surface concentrations of CO_2 and HCO_3^- and thus catalytic CO_2R and HER rates as a function of eight variables: four rate constant pre-factors and four charge transfer coefficients. This approach yielded a system of two linear equations, due to the absence of coupling steps between CO_2 and HCO_3^-, which could then be fit to experimental data (full equations available in **Supporting Information**).

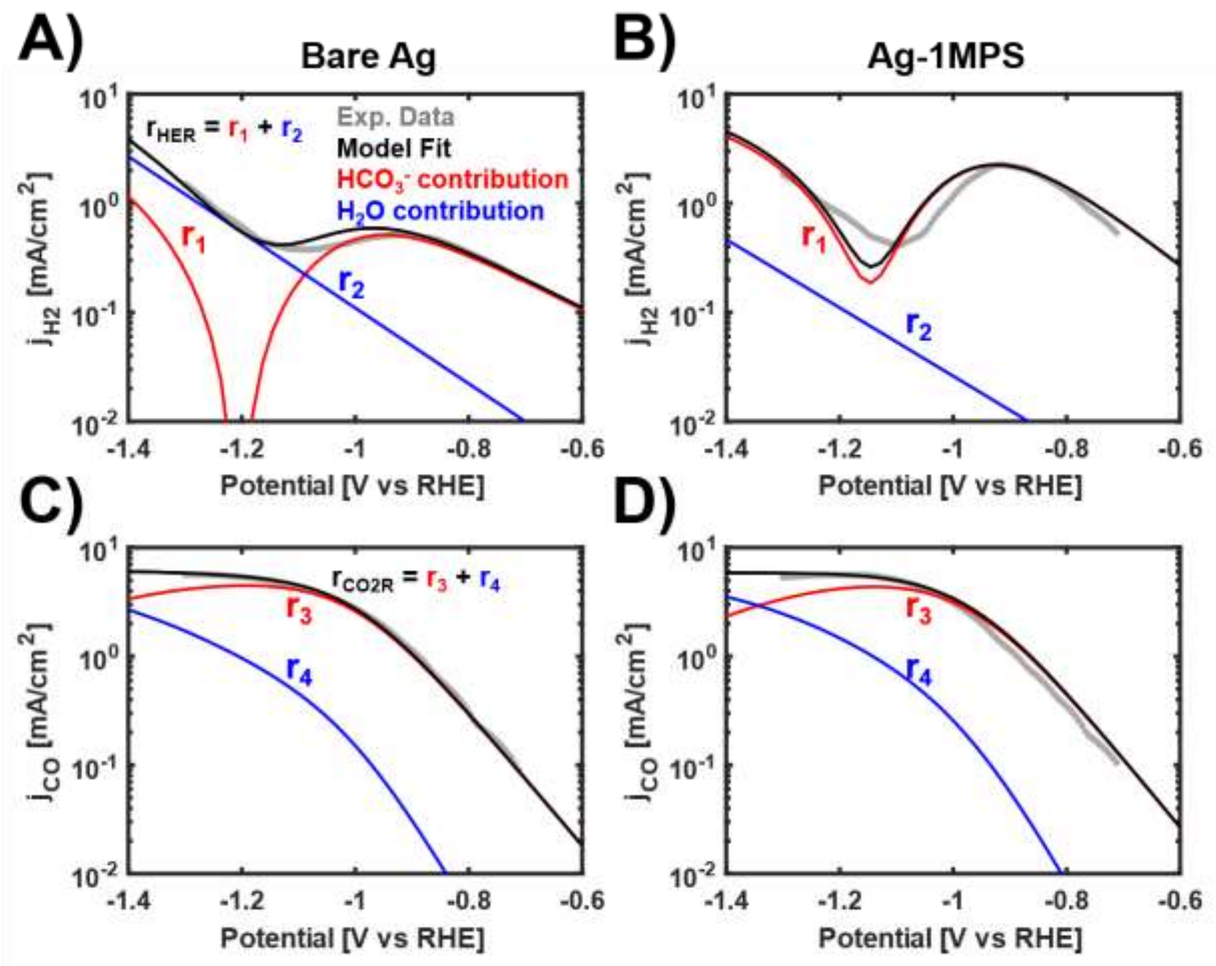

Figure 5. Partial current density to H_2 (j_{H2}, logscale) with experimental (gray), model fit (black), bicarbonate contribution to HER current (r_1, red) and H_2O contribution to HER current (r_2, blue) for bare Ag (A) and Ag-1MPS (B) with corresponding CO partial current density for bare Ag (C) and Ag-1MPS (D) with bicarbonate contribution (r_3, red) and water contribution (r_4, blue) denoted.

It is important to note the key simplifications made in this model. First, this model does not contain the full set of coupled rate equations for the CO_2/H_2O equilibria and assumes a constant boundary layer pH (by setting OH^- constant to the bulk pH value at the given [HCO_3^{-o}] and [CO_2^{o}]) which limits the quantitative accuracy of the predicted surface concentrations. This model also does not account for electromigration terms that would be expected to alter the rates of charged species at high overpotentials and high surface charges. Particularly, anionic species such as HCO_3^- and CO_3^{2-} are likely to be electrostatically repelled by the electrode at these potentials making the diffusion transport flux an overestimate which lessens the predicted effect of the bicarbonate transport limitation. In addition, this kinetic model, along with the associated kinetic experiments, cannot explicitly account for the relative contributions of different proton donors to the CO_2R pathway because of the zero-order dependence on [HCO_3^-] (**Fig 4C, 4D**) so the effect of the ionomer in promoting H_2O versus HCO_3^- reduction at high overpotentials is not fully elucidated by this analysis. Finally, this model assumes perfect first order reaction kinetics for CO_2R and HER which does not take into account the multistep reaction mechanisms for both products that could lead to more complex rate laws.

The results from fitting this kinetic model to the experimental Ag and Ag-1MPS production formation rates show the success of the model in semi-quantitatively capturing the non-monotonic "bump" feature for HER and the CO_2R profile (**Fig 5A-D**, fitted values available in **SI-Table 1** and **SI-Table 2**). The model explicitly shows this feature can arise from a competition for HCO_3^- that causes the HER from bicarbonate rate (r_1) to decline strongly as bicarbonate is depleted by increasing CO_2R rates (r_3) before water reduction compensates at higher overpotentials (r_2, r_4). In addition, it confirms the hypothesis that increasing HER rates by raising the rate for proton transfer from HCO_3^- greatly increases the size of the non-monotonic feature thus suggesting that the 1MPS ionomer layer affects this particular step in the reaction network (**Figure 5A, 5B**). The fitted values show that the rate constant for this step is ~3x larger on Ag-1MPS relative to Ag (all fitted values available in **SI-Table 1, 2**). This model can also qualitatively recover all of the main features of the aforementioned P_{CO2} and HCO_3^- concentration dependence experiments by adjusting the bulk [HCO_3^{-o}] and [CO_2^{o}] values (**SI-Figure 9-12**). In brief, the model predicts that the non-monotonic "bump" will gradually disappear at reduced CO_2 partial pressure and that HER rates would be strongly sensitive to bicarbonate concentration, [HCO_3^{-o}].

In summary, combining a kinetic model with concentration-dependent kinetic measurements supports the hypothesis that HER on Ag derives from HCO_3^- at low overpotentials and that the 1MPS ionomer layer served to increase the rate constant for this proton transfer, thus yielding higher HER rates.

Dependence of HER promotion on imidazolium functionalization

With the understanding that the 1MPS ionomer affects CO_2R on Ag primarily by promoting HER from bicarbonate, we next tested a series of imidazolium-based ionomers with different functionalities to determine if HER promotion was sensitive to small changes to ionomer structure. The ionomers 12DMPS, 1tBPS, 1BPS, and 1BzPS were tested at the same mass loading of 0.5 μg/cm^2 on Ag foil to specifically test the effect of changing the alkyl substituent on the imidazolium ring (**Fig 6A, 6B**).

These experiments again showed that imidazolium ionomers did not measurably affect CO_2R to CO rates, consistent with the results on 1MPS (**Fig 6B**). However, the different ionomers did show significant changes to the HER profiles in the region of the non-monotonic "bump"; the profiles were offset vertically with 1MPS promoting HER the most and further substitution onto the ring reducing the promotional effect (**Fig 6A**). Qualitatively, the more substituents (comparing 1MPS to 12DMPS) or the bulkier the substituent (comparing 1MPS to 1 tBPS) led to a weaker promotional effect.

We next tried to obtain quantitative understanding for the effect of imidazole substituent on HER promotion. Based on the results of the CO_2R mechanistic analysis described earlier, we believe that the early part of the j_{H2}-V curve is dominated by HCO_3^- reduction. This same region is where ionomers show the strongest effect on promoting HER rates. Thus, we hypothesize that by fitting a basic, exponential rate expression to the early part of each of the ionomer HER curves we could obtain estimates of the intrinsic bicarbonate-reduction HER rate (r_1). This fitting was performed to the functional form $j = k_0 10^{-AV}$ to obtain rate pre-factors, k_0, and potential-scaling coefficients, A, that act on the potential, V, for each of the ionomers (**Fig 6C**). The A values, analogous to α the charge transfer coefficient, are roughly independent of ionomer structure suggesting a similar rate-determining step with all ionomers. In contrast, k_0, representing the intrinsic transition state energetics for bicarbonate reduction in the presence of an ionomer, change with structure with a reduction in value with bulkier substituents in the order of 1MPS>1BPS ≈ 1BzPS > 1tBPS.

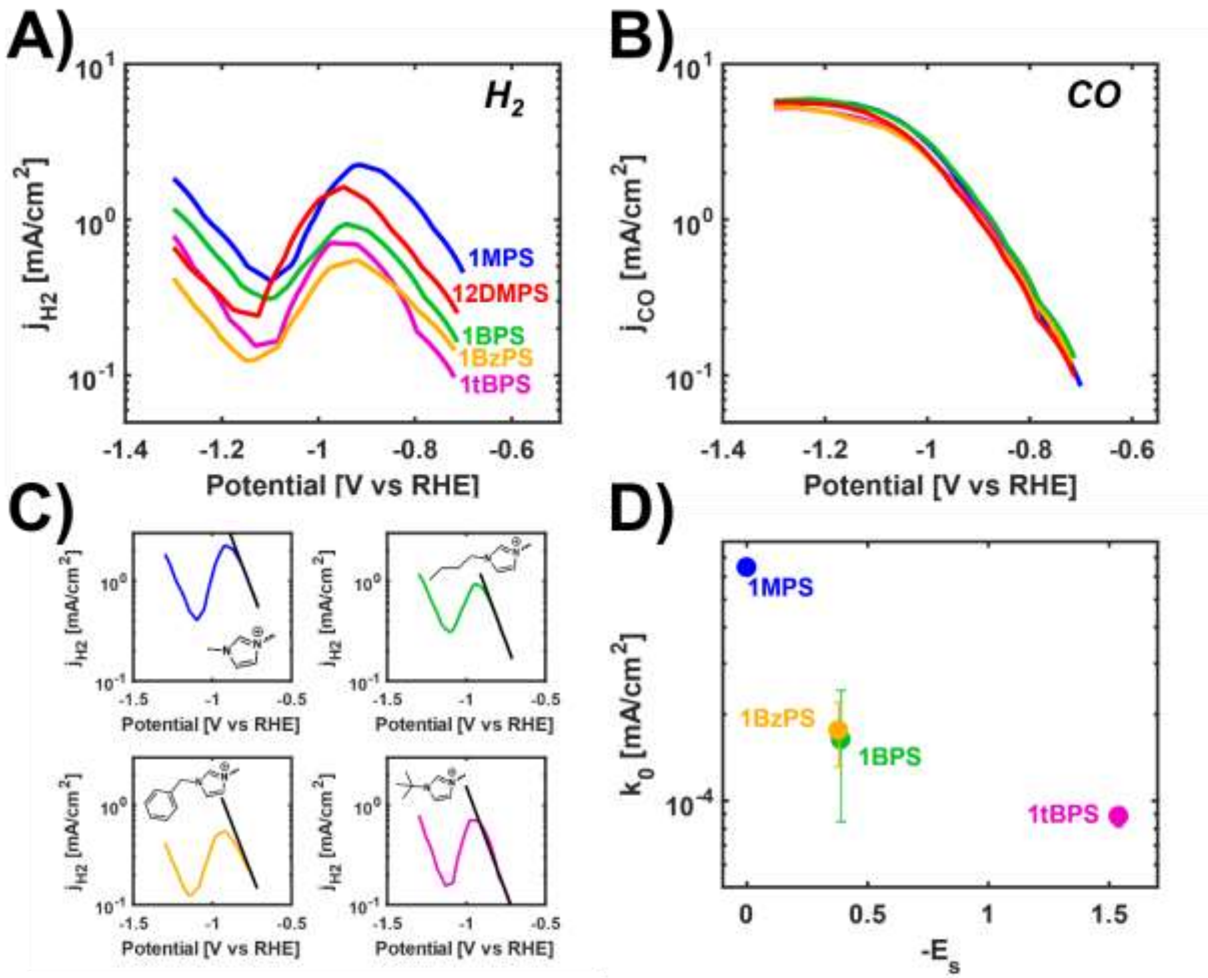

Figure 6. (A) Partial current density to H_2 (j_{H2}) vs electrode potential in logscale for a series of functionalized imidazolium-ionomers using abbreviations from **Fig 1B** and (B) corresponding CO partial current density. (C) Fits of $j = k_0 10^{-AV}$ to early part of j_{H2} curve for 1MPS (top left), 1BPS (top right), 1BzPS (bottom left), and 1tBPS (bottom right) and (D) Fitted k_0 values plotted in logscale versus $-E_s$, the steric Taft parameter.

This effect with bulkier substituents could be attributed to either electronic effects that stabilize the imidazolium cationic charge due to larger, more electron donating groups or due to a steric effect that controls the ability of the ionomer to interact with species during CO_2R. These differences in HER rates, though experimentally measurable, result from very small differences in the transition state energetics on the order of 10-50 meV. To illustrate this, comparing the rate constants for bicarbonate reduction to HER between Ag and Ag-1MPS yields a ~3x difference in rate constant which corresponds to a $\Delta(\Delta G^{\ddagger})$ (change in transition state energy) of ~0.03 eV which is challenging for the precision of typical quantum mechanical methods.

Thus, to interpret the subtle differences corresponding to the promotion of HER by ionomer layers we utilized Hammett-Taft analysis which, by measurement of rates and equilibrations of organic reactions with a variety of functional groups, can quantitatively interpret the effect of substitution on reactions.[47,48] In this framework, Hammett parameters (σ) with associated sensitivity parameter (ρ) are used for explaining electronic effects and Taft parameters (E_s) with associated sensitivity parameter (δ) to explain steric effects on reaction rate constants (k) relative to the rate constant of a reference molecule (k_0) (**Eq. 7**).

$$\ln(k/k_0) = \rho\sigma + \delta E_s \quad \textbf{Eq. 7}$$

We find that Hammett parameters, tabulated for both meta (σ_m) and para (σ_p) substituents are nearly identical for the four substituents methyl, butyl, benzyl, and tert-butyl (**Table 1**), though the 'meta' and 'para' denominations are not explicitly applicable to the imidazolium system in question.[47] Prior literature also concluded a single set of Hammett parameters should be used for all alkyl substituents due to inherent error in Hammett parameter measurement.[49] We conclude that electronic effects imparted by alkyl imidazolium substituents are unlikely to govern the differences in HER promotion observed in this study. In contrast, Taft steric parameters (E_s) vary greatly for the substituents in question and show a monotonic relationship with k_0 with the least bulky group, methyl, showing the highest HER promotion and the bulkiest group, tert-butyl, showing the smallest HER promotion (**Table 1**, **Fig 6D**). The Taft parameters also successfully predict that butyl and benzyl groups should have very similar steric effects on rate which directly agrees with experimental results of nearly identical k_0 for 1BPS and 1BzPS. Thus, the promotion of HER by imidazolium-ionomer layers seems to be particularly sensitive to steric bulk at the 1-position on the imidazolium ring.

Table 1. Fitted k_0 and A values from fit of $j = k_0 10^{-AV}$ to early part of HER curves for four polymers, 1MPS, 1BPS, 1BzPS, and 1tBPS **(Fig 6C)** with corresponding meta (σ_m) and para (σ_m) Hammett parameters[47] and steric Taft parameters (E_s)[50]

	k_0 x 10^{-4} [mA/cm^2]	A [1/V]	σ_m	σ_p	$-E_s$
1MPS	6.5 ± 0.1	4.11	-0.07	-0.17	0
1BPS	1.6 ± 0.8	4.24	-0.08	-0.16	0.39
1BzPS	1.7 ± 0.4	4.24	-0.08	-0.09	0.38
1tBPS	0.9 ± 0.1	4.07	-0.1	-0.2	1.54

Quantum chemical evidence for effect of functionalization on HER promotion by imidazolium ionomers

Finally, we employed hybrid density functional theory (DFT) to assess our hypothesis that steric bulk on imidazolium ionomers modulates the rates of bicarbonate at Ag surfaces. These calculations were performed using a potential-controlled implicit solvation environment mimicking a 0.1 M electrolyte solution with a styrene-imidazolium model of the ionomer on the Ag (100) electrode surface, a surface facet known to be important in the electrochemical behavior of polycrystalline Ag.[44,51] We refer the reader to the Simulation Methods section for comprehensive details on the calculation set up. Using this model, we calculated the thermodynamic reaction free energy of Ag mediated bicarbonate deprotonation (**Eq. 4**) in the presence of the styrene-imidazolium molecule containing either 1-methylimidazole (Ag-1MPS) or 1-tertbutylimidazole (Ag-1tBPS). Adsorbed HCO_3* was investigated as the reactant which is motivated by prior *in situ* infrared spectroscopy studies that suggest that anions such as phosphate, carboxylate, and carbonate can be adsorbed and in the near-surface region at negative electrode potentials during CO_2R.[52,53]

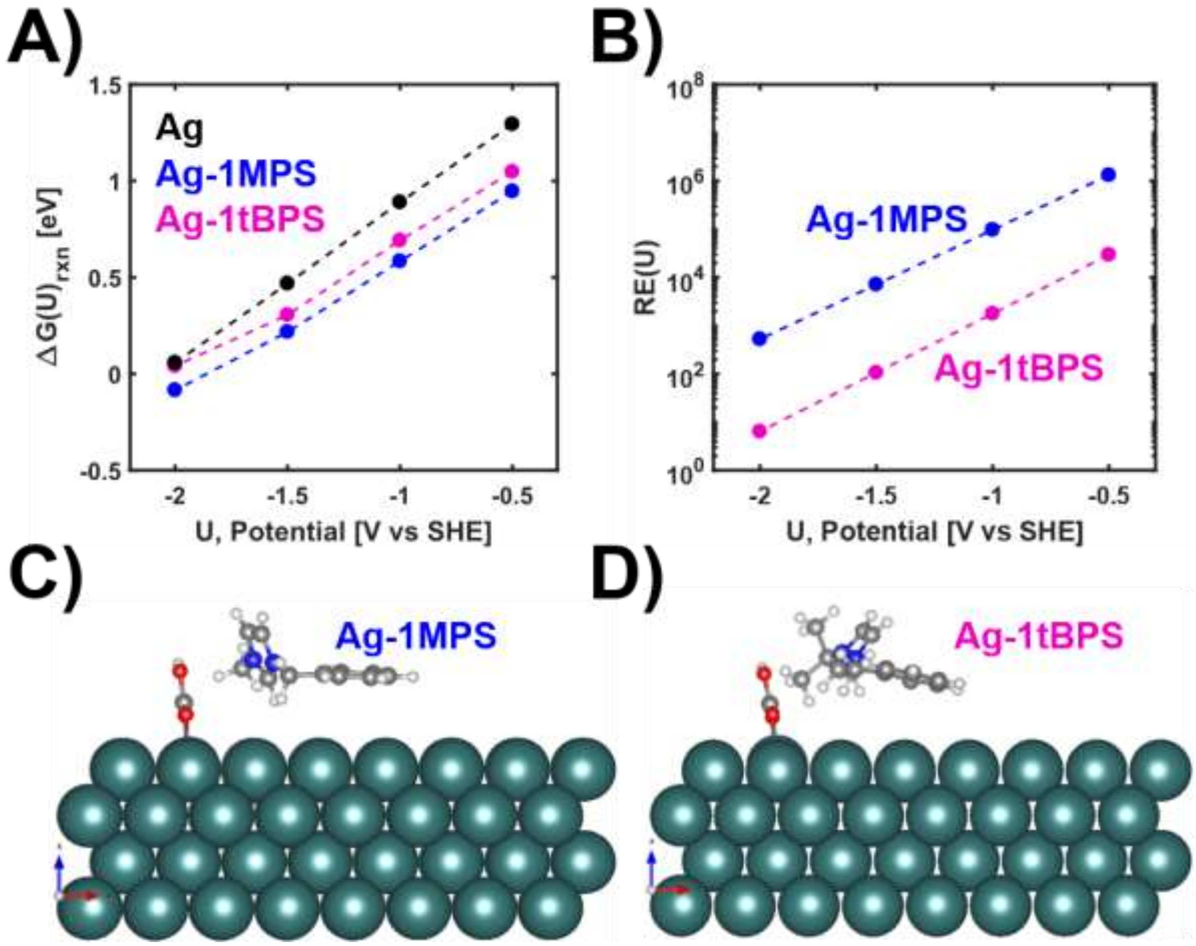

Figure 7. (A) Potential-dependent reaction free energies (eV) of bicarbonate deprotonation, computed using **Eq. 5**, on the bare Ag(100) surface (•) and with 1tBPS (•) and 1MPS (•) present. (B) Relative promotion in the thermodynamic rate of bicarbonate deprotonation due to 1MPS and 1tBPS computed using **Eq. 6**. Profile view of DFT optimized structures of (C) HCO_3 + 1MPS and (D) HCO_3 + 1tBPS on Ag (100) computed at −0.5 V vs SHE. Atom color representations: hydrogen (light gray), carbon (dark gray), oxygen (red), nitrogen (blue) and silver (teal).

The thermodynamic reaction free energy for hydrogen transfer from HCO_3* is reduced in the presence of both imidazolium molecules relative to the bare Ag surface when no ionomer additive is present, from ~1.29 eV (no ionomer additive) to 1.05 eV and 0.95 eV for Ag-1tBPS and Ag-1MPS respectively at -0.5 V vs SHE (**Fig 7A**). These thermodynamic reaction free energies scale linearly with potential and predict that HER will proceed in the order 1-methylimidazolium > 1-tertbutylimidazolium >> bare Ag surface. These results predict that 1) imidazolium moieties could serve to greatly reduce the barriers for bicarbonate reduction and 2) the 1-methylimidazolium polymer, 1MPS, would be predicted to promote HER more than the bulkier 1-tertbutylimidazolium polymer, 1tBPS, both in agreement with the experimental findings (**Fig 6D, Fig 7A**). The relative promotional effect in the rate of hydrogen transfer (RE(U), **Eq. 6**), by accounting for the ratio of the Boltzmann factors, indicates a 1-2 orders of magnitude increase in the case of Ag-1MPS over Ag-1tBPS (**Fig 7B**). This enhancement is quantitatively higher than the promotion of bicarbonate-derived HER that is observed experimentally and can be attributed in part due to estimation of these energetics only on pristine Ag (100) surfaces and not accounting for the influence of surface coverage of other participating species and the ionomer itself. For instance, the large steric bulk of the backbone and 30 at% ionic group concentration might prevent imidazolium species from interacting with many Ag surface sites simultaneously, leading to experimental measurements that reflect a distribution of sites and associated rates that is not easily captured by the quantum chemical calculation. The computed free energies moreover stand as proxies for activation barriers for bicarbonate deprotonation assuming a Brønsted–Evans–Polanyi (BEP) correlation exists with the transition state scaling linearly with the computed free energies in this study.[54–56] The validity of such correlations in ionomer promoted systems is the subject of a future study.

The DFT calculations can also shed light on the role of sterics in governing the HER promotion activity via comparison of the computed geometries between the 1-methylimidazolium-styrene and 1-tertbutylimidazolium-styrene cases. Both molecules are predicted to have the styrene lie flat against the surface with the imidazolium group interacting with the HCO_3* reactant and CO_3* product (**Fig 7C,7D**). However, the proximity of the imidazolium is limited by the bulkiness of the 1-position substituent resulting in a larger interatomic $N_{imidazole}$–O_{HCO3} distance of 5.31 Å for 1-tertbutyl relative to 4.88 Å for 1-methylimidazolium (**Fig 7C,7D**). These results suggest that the steric bulk impacts ionomer promotion by limiting accessibility, and thus reducing stabilization that enables the higher apparent acidity of HCO_3^-. In addition to the steric effect, the promotional effect of the ionomer can be further understood by examining the differences in the interfacial charge density due to the presence of the ionomers (**SI-Figure 14**), wherein a higher degree of electron gain is observed in the imidazolium ring of the 1MPS relative to 1tBPS and correlates to the proximity of the 2*p* orbitals of the oxygen atoms (O_{HCO3}) with the imidazolium ring. Further, a π-π orbital overlap between the surface Ag atoms and the styrene monomer ring in 1MPS promotes interfacial charge transfer from the metal to the styrene ring. This effect is reduced with 1tBPS due to steric hindrance of the methyl substituents that decreases π-π orbital overlap. The extent of π-π orbital overlap manifests as an electronic effect where a slight negative shift in the potential of zero-charge (PZC) of the Ag surface of 85 meV (Ag-1MPS) and 76 (Ag-1tBPS) is obtained when the ionomer is in close proximity to the Ag surface. We hypothesize that the positively charged ionomer could electrostatically stabilize the anionic transition state of the $HCO_3^- \rightarrow H^+ + CO_3^{2-}$ reaction, thus increasing HCO_3^- reduction rates for HER. Further experimental evidence for direct interaction between ionomer and HCO_3^-/CO_3^{2-} is necessary to confirm this hypothesis.

Conclusion

The above results show that imidazolium-containing ionomers intrinsically promote HER on Ag under CO_2R conditions and have no measurable effect on CO_2R to CO kinetics in contrast to expectations based on prior literature. This promotion of HER manifests in the low overpotential regime which is followed by a decrease in j_{H2} before resumption of Tafel HER kinetics leading to a pronounced, non-monotonic "bump" in the HER current profile vs potential. This non-monotonic HER profile, also observed on bare Ag, is explained here for the first time, through CO_2 and $KHCO_3$ concentration-dependence experiments and microkinetic modeling, as a phenomenon resulting from the competition for the bicarbonate, HCO_3^-, proton donor between CO_2R and HER. This conclusion allows us to identify that the promotion of HER on Ag from imidazolium-containing ionomers originates from an increase in rate of the bicarbonate proton-donor pathway and that the insensitivity of CO_2R rates results from a CO_2R rate-determining step that does not include proton transfer.

Interestingly, functionalization of the imidazolium-ring at the 1-position with a series of alkyl functional groups has a marked impact on the promotion of the bicarbonate-derived HER pathway. Kinetic parameters for bicarbonate-derived HER on Ag in the presence of these ionomers show that the steric Taft parameter is a good descriptor for HER promotion suggesting that increased steric bulk reduced the ability for the ionomers to interact with the Ag surface or HCO_3^-/CO_3^{2-} and thus facilitate proton transfer. These results are corroborated by density functional theory (DFT) calculations that predict more favorable reaction energetics for HCO_3^- reduction in the presence of imidazolium species and show that proximity of the imidazole to the Ag surface and HCO_3 underlies this stabilization.

This work conclusively shows that ionomers can exert strong control on reaction pathways in CO_2R and, though in this case shown for the typically undesired HER, can selectively promote certain product pathways without effect on others. In terms of ionomer design rules, these results suggest that future CO_2R ionomer discovery efforts should 1) quantify and optimize steric bulk of substituents, 2) incorporate more complex substituents than alkyl groups and, 3) continue to explore non-imidazolium cationic groups. The direct influence of ionomer structure on tuning this promoter effect opens the door for a myriad of future studies that incorporate changes to molecular weight, backbone chemistry, ionic group density and ionic group structure that could play a vital role in suppressing HER and steering selectivity between different products in the complex Cu-catalyzed CO_2R product distribution. Further design of this CO_2R ionomer-catalyst interface could ultimately lead to optimized membrane-electrode-assembly CO_2 electrolyzers that produce carbon-neutral products at industrial scale.

Supporting Information: ^{1}H NMR of ionomers, XPS spectra, kinetic model parameters and comparison to catalytic data (pdf file), DFT-optimized coordinates and energies (zip file)

Acknowledgements

This work was supported by a cooperative research and development agreement among Lawrence Livermore National Laboratory, Stanford University and TOTAL American Services, Inc. (affiliate of TOTAL SE) under agreement number TC02307. In addition, support was provided by the U.S. Department of Energy, Office of Science, Office of Basic Energy Sciences, Chemical Sciences, Geosciences, and Biosciences Division, Catalysis Science Program to the SUNCAT Center for Interface Science and Catalysis. Part of this work was performed at the Stanford Nano Shared Facilities (SNSF), supported by the National Science Foundation under award ECCS-2026822. The authors thank Dr. Jiancheng Lai for GPC and Dr. Stacey Bent for ellipsometry and Dr. Penghao Xiao for design and implementation of electrochemical potential controlled simulations module in VASP.

References

(1) Billmeyer, F. *Textbook of Polymer Science*; John Wiley & Sons, 1962.

(2) Landel, R.F., Nielsen, L. E. *Mechanical Properties of Polymers and Composites*, 2nd ed.; Taylor & Francis Group: Boca Raton, FL, 1993.

(3) Blom, P. W. M. Polymer Electronics: To Be or Not to Be? *Adv. Mater. Technol.* **2020**, *5* (6), 1–14. https://doi.org/10.1002/admt.202000144.

(4) Maitz, M. F. Applications of Synthetic Polymers in Clinical Medicine. *Biosurface and Biotribology* **2015**, *1* (3), 161–176. https://doi.org/10.1016/j.bsbt.2015.08.002.

(5) Adhikari, S.; Pagels, M. K.; Jeon, J. Y.; Bae, C. Ionomers for Electrochemical Energy Conversion & Storage Technologies. *Polymer (Guildf).* **2020**, *211* (September), 123080. https://doi.org/10.1016/j.polymer.2020.123080.

(6) Kusoglu, A.; Weber, A. Z. New Insights into Perfluorinated Sulfonic-Acid Ionomers. *Chem. Rev.* **2017**, *117* (3), 987–1104. https://doi.org/10.1021/acs.chemrev.6b00159.

(7) Chen, N.; Lee, Y. M. Anion Exchange Polyelectrolytes for Membranes and Ionomers. *Prog. Polym. Sci.* **2021**, *113*, 101345. https://doi.org/10.1016/j.progpolymsci.2020.101345.

(8) Visser, S. P. Second-Coordination Sphere Effects on Selectivity and Specificity of Heme and Nonheme Iron Enzymes. *Chem. – A Eur. J.* **2020**, *26* (24), 5308–5327.

https://doi.org/10.1002/chem.201905119.

(9) Shook, R. L.; Borovik, A. S. Role of the Secondary Coordination Sphere in Metal-Mediated Dioxygen Activation. *Inorg. Chem.* **2010**, *49* (8), 3646–3660. https://doi.org/10.1021/ic901550k.

(10) Hahn, C.; Jaramillo, T. F. Using Microenvironments to Control Reactivity in CO2 Electrocatalysis. *Joule* **2020**, *4* (2), 292–294. https://doi.org/10.1016/j.joule.2020.01.017.

(11) Fu, Q.; Bao, X. Confined Microenvironment for Catalysis Control. *Nat. Catal.* **2019**, *2* (10), 834–836. https://doi.org/10.1038/s41929-019-0354-z.

(12) De Luna, P.; Hahn, C.; Higgins, D.; Jaffer, S. A.; Jaramillo, T. F.; Sargent, E. H. What Would It Take for Renewably Powered Electrosynthesis to Displace Petrochemical Processes? *Science (80-.).* **2019**, *364* (6438), eaav3506. https://doi.org/10.1126/science.aav3506.

(13) Ohma, A.; Fushinobu, K.; Okazaki, K. Influence of Nafion® Film on Oxygen Reduction Reaction and Hydrogen Peroxide Formation on Pt Electrode for Proton Exchange Membrane Fuel Cell. *Electrochim. Acta* **2010**, *55* (28), 8829–8838. https://doi.org/10.1016/j.electacta.2010.08.005.

(14) Nam, D.-H.; De Luna, P.; Rosas-Hernández, A.; Thevenon, A.; Li, F.; Agapie, T.; Peters, J. C.; Shekhah, O.; Eddaoudi, M.; Sargent, E. H. Molecular Enhancement of Heterogeneous CO2 Reduction. *Nat. Mater.* **2020**, *19* (3), 266–276. https://doi.org/10.1038/s41563-020-0610-2.

(15) Zhang, S.; Kang, P.; Ubnoske, S.; Brennaman, M. K.; Song, N.; House, R. L.; Glass, T.; Meyer, T. J. Polyethylenimine-Enhanced Electrocatalytic Reduction of CO 2 to Formate at Nitrogen-Doped Carbon Nanomaterials. **2014**. https://doi.org/10.1021/ja5031529.

(16) Thevenon, A.; Rosas-Hernández, A.; Fontani Herreros, A. M.; Agapie, T.; Peters, J. C. Dramatic HER Suppression on Ag Electrodes via Molecular Films for Highly Selective CO 2 to CO Reduction. *ACS Catal.* **2021**, 4530–4537. https://doi.org/10.1021/acscatal.1c00338.

(17) Kramer, W. W.; McCrory, C. C. L. Polymer Coordination Promotes Selective CO 2 Reduction by Cobalt Phthalocyanine. *Chem. Sci.* **2016**, *7* (4), 2506–2515. https://doi.org/10.1039/C5SC04015A.

(18) Kutz, R. B.; Chen, Q.; Yang, H.; Sajjad, S. D.; Liu, Z.; Masel, I. R. Sustainion Imidazolium-Functionalized Polymers for Carbon Dioxide Electrolysis. *Energy Technol.* **2017**, *5* (6), 929–936. https://doi.org/10.1002/ente.201600636.

(19) Liu, Z.; Yang, H.; Kutz, R.; Masel, R. I. CO 2 Electrolysis to CO and O 2 at High Selectivity, Stability and Efficiency Using Sustainion Membranes. *J. Electrochem. Soc.* **2018**, *165* (15), J3371–J3377. https://doi.org/10.1149/2.0501815jes.

(20) Lau, G. P. S.; Schreier, M.; Vasilyev, D.; Scopelliti, R.; Grätzel, M.; Dyson, P. J. New Insights into the Role of Imidazolium-Based Promoters for the Electroreduction of CO2 on a Silver Electrode. *J. Am. Chem. Soc.* **2016**, *138* (25), 7820–7823. https://doi.org/10.1021/jacs.6b03366.

(21) Zhao, S.-F.; Horne, M.; Bond, A. M.; Zhang, J. Is the Imidazolium Cation a Unique

Promoter for Electrocatalytic Reduction of Carbon Dioxide? *J. Phys. Chem. C* **2016**, *120* (42), 23989–24001. https://doi.org/10.1021/acs.jpcc.6b08182.

(22) Sung, S.; Kumar, D.; Gil-Sepulcre, M.; Nippe, M. Electrocatalytic CO 2 Reduction by Imidazolium-Functionalized Molecular Catalysts. *J. Am. Chem. Soc.* **2017**, *139* (40), 13993–13996. https://doi.org/10.1021/jacs.7b07709.

(23) Han, Z.; Kortlever, R.; Chen, H.-Y.; Peters, J. C.; Agapie, T. CO 2 Reduction Selective for C ≥2 Products on Polycrystalline Copper with N-Substituted Pyridinium Additives. *ACS Cent. Sci.* **2017**, *3* (8), 853–859. https://doi.org/10.1021/acscentsci.7b00180.

(24) Li, F.; Thevenon, A.; Rosas-Hernández, A.; Wang, Z.; Li, Y.; Gabardo, C. M.; Ozden, A.; Dinh, C. T.; Li, J.; Wang, Y.; et al. Molecular Tuning of CO2-to-Ethylene Conversion. *Nature* **2020**, *577* (7791), 509–513. https://doi.org/10.1038/s41586-019-1782-2.

(25) Wang, J.; Cheng, T.; Fenwick, A. Q.; Baroud, T. N.; Rosas-Hernández, A.; Ko, J. H.; Gan, Q.; Goddard III, W. A.; Grubbs, R. H. Selective CO 2 Electrochemical Reduction Enabled by a Tricomponent Copolymer Modifier on a Copper Surface. *J. Am. Chem. Soc.* **2021**, *143* (7), 2857–2865. https://doi.org/10.1021/jacs.0c12478.

(26) García de Arquer, F. P.; Dinh, C. T.; Ozden, A.; Wicks, J.; McCallum, C.; Kirmani, A. R.; Nam, D. H.; Gabardo, C.; Seifitokaldani, A.; Wang, X.; et al. CO2 Electrolysis to Multicarbon Products at Activities Greater than 1 A Cm−2. *Science (80-.).* **2020**, *367* (6478), 661–666. https://doi.org/10.1126/science.aay4217.

(27) Lobaccaro, P.; Singh, M. R.; Clark, E. L.; Kwon, Y.; Bell, A. T.; Ager, J. W. Effects of Temperature and Gas–Liquid Mass Transfer on the Operation of Small Electrochemical

Cells for the Quantitative Evaluation of CO 2 Reduction Electrocatalysts. *Phys. Chem. Chem. Phys.* **2016**, *18* (38), 26777–26785. https://doi.org/10.1039/C6CP05287H.

(28) Hatsukade, T.; Kuhl, K. P.; Cave, E. R.; Abram, D. N.; Jaramillo, T. F. Insights into the Electrocatalytic Reduction of CO2 on Metallic Silver Surfaces. *Phys. Chem. Chem. Phys.* **2014**, *16* (27), 13814–13819. https://doi.org/10.1039/c4cp00692e.

(29) Kresse, G.; Hafner, J. Ab Initio Molecular Dynamics for Liquid Metals. *Phys. Rev. B* **1993**, *47* (1), 558–561. https://doi.org/10.1103/PhysRevB.47.558.

(30) Kresse, G.; Furthmüller, J. Efficient Iterative Schemes for Ab Initio Total-Energy Calculations Using a Plane-Wave Basis Set. *Phys. Rev. B* **1996**, *54* (16), 11169–11186. https://doi.org/10.1103/PhysRevB.54.11169.

(31) Blöchl, P. E. Projector Augmented-Wave Method. *Phys. Rev. B* **1994**, *50* (24), 17953–17979. https://doi.org/10.1103/PhysRevB.50.17953.

(32) Hammer, B.; Hansen, L. B.; Nørskov, J. K. Improved Adsorption Energetics within Density-Functional Theory Using Revised Perdew-Burke-Ernzerhof Functionals. *Phys. Rev. B* **1999**, *59* (11), 7413–7421. https://doi.org/10.1103/PhysRevB.59.7413.

(33) Perdew, J. P.; Chevary, J. A.; Vosko, S. H.; Jackson, K. A.; Pederson, M. R.; Singh, D. J.; Fiolhais, C. Atoms, Molecules, Solids, and Surfaces: Applications of the Generalized Gradient Approximation for Exchange and Correlation. *Phys. Rev. B* **1993**, *48* (7), 4978–4978. https://doi.org/10.1103/PhysRevB.48.4978.2.

(34) Methfessel, M.; Paxton, A. T. High-Precision Sampling for Brillouin-Zone Integration in

Metals. *Phys. Rev. B* **1989**, *40* (6), 3616–3621. https://doi.org/10.1103/PhysRevB.40.3616.

(35) Grimme, S.; Antony, J.; Ehrlich, S.; Krieg, H. A Consistent and Accurate Ab Initio Parametrization of Density Functional Dispersion Correction (DFT-D) for the 94 Elements H-Pu. *J. Chem. Phys.* **2010**, *132* (15), 154104. https://doi.org/10.1063/1.3382344.

(36) Fishman, M.; Zhuang, H. L.; Mathew, K.; Dirschka, W.; Hennig, R. G. Accuracy of Exchange-Correlation Functionals and Effect of Solvation on the Surface Energy of Copper. *Phys. Rev. B* **2013**, *87* (24), 245402. https://doi.org/10.1103/PhysRevB.87.245402.

(37) Mathew, K.; Sundararaman, R.; Letchworth-Weaver, K.; Arias, T. A.; Hennig, R. G. Implicit Solvation Model for Density-Functional Study of Nanocrystal Surfaces and Reaction Pathways. *J. Chem. Phys.* **2014**, *140* (8), 084106. https://doi.org/10.1063/1.4865107.

(38) Duan, Z.; Xiao, P. Simulation of Potential-Dependent Activation Energies in Electrocatalysis: Mechanism of O–O Bond Formation on RuO 2. *J. Phys. Chem. C* **2021**, *125* (28), 15243–15250. https://doi.org/10.1021/acs.jpcc.1c02998.

(39) Weber, R. L.; Ye, Y.; Banik, S. M.; Elabd, Y. A.; Hickner, M. A.; Mahanthappa, M. K. Thermal and Ion Transport Properties of Hydrophilic and Hydrophobic Polymerized Styrenic Imidazolium Ionic Liquids. *J. Polym. Sci. Part B Polym. Phys.* **2011**, *49* (18), 1287–1296. https://doi.org/10.1002/polb.22319.

(40) Paulus, U. A.; Schmidt, T. J.; Gasteiger, H. A.; Behm, R. J. Oxygen Reduction on a High-Surface Area Pt/Vulcan Carbon Catalyst: A Thin-Film Rotating Ring-Disk Electrode Study. *J. Electroanal. Chem.* **2001**, *495* (2), 134–145. https://doi.org/10.1016/S0022-0728(00)00407-1.

(41) Hugar, K. M.; Kostalik, H. A.; Coates, G. W. Imidazolium Cations with Exceptional Alkaline Stability: A Systematic Study of Structure–Stability Relationships. *J. Am. Chem. Soc.* **2015**, *137* (27), 8730–8737. https://doi.org/10.1021/jacs.5b02879.

(42) Rosen, B. A.; Salehi-Khojin, A.; Thorson, M. R.; Zhu, W.; Whipple, D. T.; Kenis, P. J. A.; Masel, R. I. Ionic Liquid-Mediated Selective Conversion of CO2 to CO at Low Overpotentials. *Science (80-.).* **2011**, *334* (6056), 643–644. https://doi.org/10.1126/science.1209786.

(43) Clark, E. L.; Bell, A. T. Direct Observation of the Local Reaction Environment during the Electrochemical Reduction of CO 2. *J. Am. Chem. Soc.* **2018**, *140* (22), 7012–7020. https://doi.org/10.1021/jacs.8b04058.

(44) Clark, E. L.; Ringe, S.; Tang, M.; Walton, A.; Hahn, C.; Jaramillo, T. F.; Chan, K.; Bell, A. T. Influence of Atomic Surface Structure on the Activity of Ag for the Electrochemical Reduction of CO 2 to CO. *ACS Catal.* **2019**, *9* (5), 4006–4014. https://doi.org/10.1021/acscatal.9b00260.

(45) Resasco, J.; Lum, Y.; Clark, E.; Zeledon, J. Z.; Bell, A. T. Effects of Anion Identity and Concentration on Electrochemical Reduction of CO 2. *ChemElectroChem* **2018**, *5* (7), 1064–1072. https://doi.org/10.1002/celc.201701316.

(46) Zeng, J. S.; Corbin, N.; Williams, K.; Manthiram, K. Kinetic Analysis on the Role of Bicarbonate in Carbon Dioxide Electroreduction at Immobilized Cobalt Phthalocyanine. *ACS Catal.* **2020**, *10* (7), 4326–4336. https://doi.org/10.1021/acscatal.9b05272.

(47) Hansch, C.; Leo, A.; Taft, R. W. A Survey of Hammett Substituent Constants and Resonance and Field Parameters. *Chem. Rev.* **1991**, *91* (2), 165–195. https://doi.org/10.1021/cr00002a004.

(48) Taft, R. W. Linear Steric Energy Relationships. *J. Am. Chem. Soc.* **1953**, *75* (18), 4538–4539. https://doi.org/10.1021/ja01114a044.

(49) Jaffé, H. H. A Reexamination of the Hammett Equation. *Chem. Rev.* **1953**, *53* (2), 191–261. https://doi.org/10.1021/cr60165a003.

(50) Sigman, M. S.; Miller, J. J. Examination of the Role of Taft-Type Steric Parameters in Asymmetric Catalysis. *J. Org. Chem.* **2009**, *74* (20), 7633–7643. https://doi.org/10.1021/jo901698t.

(51) Larkin, D. The Structure of the Polycrystalline Silver-Aqueous Interface. *J. Electroanal. Chem. Interfacial Electrochem.* **1983**, *157* (1), 123–128. https://doi.org/10.1016/S0022-0728(83)80380-5.

(52) Yang, K.; Kas, R.; Smith, W. A. In Situ Infrared Spectroscopy Reveals Persistent Alkalinity near Electrode Surfaces during CO2 Electroreduction. *J. Am. Chem. Soc.* **2019**, *141* (40). https://doi.org/10.1021/jacs.9b07000.

(53) Chernyshova, I. V.; Somasundaran, P.; Ponnurangam, S. On the Origin of the Elusive

First Intermediate of CO_2 Electroreduction. *Proc. Natl. Acad. Sci.* **2018**, 201802256. https://doi.org/10.1073/pnas.1802256115.

(54) Bronsted, J. N. Acid and Basic Catalysis. *Chem. Rev.* **1932**, *10* (1), 231–338. https://doi.org/10.1021/cr60035a011.

(55) Evans, M. G.; Polanyi, M. Inertia and Driving Force of Chemical Reactions. *Trans. Faraday Soc.* **1938**, *34*, 11–24.

(56) Wang, S.; Vorotnikov, V.; Sutton, J. E.; Vlachos, D. G. Brønsted–Evans–Polanyi and Transition State Scaling Relations of Furan Derivatives on Pd(111) and Their Relation to Those of Small Molecules. *ACS Catal.* **2014**, *4* (2), 604–612. https://doi.org/10.1021/cs400942u.

For TOC only: